Aging Effect on Functionalized Silver-Based Nanocoating Braided Coronary Stents

Rita Rebelo [1,2,3], Jorge Padrão [1] (ORCID)**, Margarida M. Fernandes [2,3], Sandra Carvalho [2,4]** (ORCID)**, Mariana Henriques [3]** (ORCID)**, Andrea Zille [1,*]** (ORCID) **and Raul Fangueiro [1]** (ORCID)

[1] 2C2T-Centre for Textile Science and Technology, University of Minho, 4800-058 Guimarães, Portugal; ritanogueirar@gmail.com (R.R.); padraoj@2c2t.uminho.pt (J.P.); rfangueiro@dem.uminho.pt (R.F.)

[2] CFUM-UP, Physics Department, Campus of Azurém, University of Minho, 4800-058 Guimarães, Portugal; margaridafernandes@fisica.uminho.pt (M.M.F.); sandra.carvalho@fisica.uminho.pt (S.C.)

[3] CEB, Centre of Biological Engineering, Campus de Gualtar, University of Minho, 4710-335 Braga, Portugal; mcrh@deb.uminho.pt

[4] SEG-CEMMPRE Mechanical Engineering Department, University of Coimbra, 3030-788 Coimbra, Portugal

[*] Correspondence: azille@2c2t.uminho.pt; Tel.: +351-253-510-285

check for updates

Abstract: A previously developed fiber-based polyester (PES) stent, with mechanical properties comparable to commercial nitinol stents, was coated with metallic silver (Ag^0) and silver oxides (Ag_xO) thin films through direct current (DC) magnetron sputtering. Ag^0 and Ag_xO coatings provide antimicrobial properties to the stents to minimize the occurrence of coronary stent infections. Nevertheless, the stent interacts with the atmosphere and then with the biological fluids and may lead to the generation of silver species with diminished antimicrobial efficiency and/or prone to induce cytotoxicity. Therefore, stent coating nanostructures aged 3 months were thoroughly analyzed by X-ray photoelectron spectroscopy (XPS) and their antimicrobial and cytotoxicity properties were assessed. Aging led to the presence of silver carbonate and bicarbonate as well as chemisorbed oxygen species in Ag^0 and Ag_xO coatings. Bactericidal efficacy was tested against an important nosocomial bacterium, particularly associated to indwelling devices: *Staphylococcus epidermidis*. Aged Ag^0 and Ag_xO coating presented a Log reduction of 1 and 2 at their surface; respectively. However, aged stents were able to induce a Log reduction of 2 (Ag^0) and 4 (Ag_xO) on the surrounding medium. Only aged Ag_xO stent was able to provide a mild reduction of the bacterium at its surface and a clear antimicrobial effect (Log reduction >3) within its vicinity. More importantly, both aged Ag^0 and Ag_xO stents were shown to be compatible with fibroblasts cells indicating that they can be safely used as indwelling devices, despite the aging effect.

Keywords: stent; silver; textile; direct current magnetron sputtering; X-ray photoelectron spectroscopy; bactericidal; cytotoxicity

1. Introduction

Cardiovascular diseases (CVD) represent nearly half of mortality in Europe, resulting each year in a loss of over €200 billion [1]. Atherosclerosis of the coronary arteries is the principal cause of CVD. It occurs when blood flow is obstructed due to cholesterol build-up within the arterial walls, causing the incidence of clot formation and severe circulatory problems [2]. Atherosclerosis treatment is mandatory and includes oral medication comprising vasodilators, anticoagulants or antiplatelet agents, as well as surgical procedures such as coronary artery bypass grafting, angioplasties and stent application [3,4]. Although angioplasties are effective in the immediate treatment of atherosclerosis, it often results in restenosis and reocclusion of arteries [5]. Instead, stenting techniques have been regarded the most

efficient approach to widen the clogged blood vessel, providing a potential long-term solution for the problem [6].

Despite the considerable advances in stent development, stent application still faces two major issues: restenosis and infection.

Stents currently commercialized are essentially made of metals or metal alloys, particularly stainless steel, due to its appropriate mechanical properties which maintain the blood vessel dilated [7]. Metallic stents, however, are prone to corrosion and restenosis. In fact, restenosis with metallic stents occurs in approximately 30% of the patients, representing a serious issue. A major cause for restenosis is the injury of blood vessels by the stent metallic rods, which trigger an immune and inflammatory response [6]. Hemorrhagic complications, thrombosis and neointimal hyperplasia have also been commonly reported during the use of bare metallic stents [8]. Coronary stent infection is considered to be rare, nevertheless it represents a severe complication with an alarmingly high mortality [9]. Bacteria may attach to the stent surface, proliferate in multilayers cohesively intertwined within a self-synthesized extracellular polymer matrix, thus forming a biofilm [10]. Biofilms are extremely hard to eliminate, due to their renowned resistance to host immune system and antibiotics and can lead to chronic inflammation at the stent location and in the organs at its vicinity, and also to bacteremia. In fact, in Europe, 87% of hospital-acquired bacteremia were associated with a venous device, resulting in grievous health complications, which commonly imply multiple surgeries and intravenous antibiotic treatment [11,12].

Extensive research is being carried out on indwelling medical devices to minimize these problems. Coating the metallic surface with polymers to improve its surface characteristics without interfering with the bulk properties of the metal stent reduce restenosis occurrence. However, as the coating is usually applied on a stent surface in its crimped state, after expansion inside the blood vessel the surface area considerably increases, which may lead to fissures, cracks and pores as well as the release of debris which later may increase the occurrence of restenosis [13]. Therefore, development of biocompatible stents that avoid corrosion and restenosis events associated to metallic stents and polymeric coatings is warranted. This research group has developed a novel 100% fiber-based polyester stent, produced through braiding technology, proven to fulfill stent mandatory requirements, namely: biocompatibility, adequate mechanical strength, radiopacity, longitudinal flexibility, ease of handling, corrosion resistance, and ability to withstand radial expansion and recovery [6,14]. Braided fibrous stents displayed greater stent visibility, flexibility and collection rate (up to 87%). Different coatings have been applied in commercially available coronary stents to enhance their properties, particularly drug-eluting stents which include in their formulation: vasodilators, anticoagulants, healing promoters, anti-proliferatives, immunosuppressants, and antimicrobials [4]. Antimicrobial compounds include zwitterionic phosphorylcholine, and rapamycin and actinomycin-D [4,15]. Nevertheless, the use of these compounds is primarily focused on their cytostatic and anti-inflammatory proprieties to prevent neointimal hyperplasia [15]. The application of a potent antimicrobial material, which is not easily susceptible to induce resistance, at the stent surface can be a viable strategy to prophylactically act against infection, particularly in pathogenic-prone environments such as hospitals [16]. This strategy has been successfully applied in ureteral stents, which are highly susceptible to microbial colonization [17,18]. Silver (Ag) is among the most notorious and widespread divalent metal antimicrobial agents [19]. Moreover, Ag can be applied as a thin film coating on the stent surface by reactive pulsed direct current (DC) magnetron sputtering [20,21]. Nevertheless, it may be considered unfeasible to apply the coated stent immediately after its production, or even within a short time span. Therefore, the stent coating may undergo aging variations which may hinder its effectiveness and applicability. This work envisages the thorough assessment of the chemical modifications that stent coatings of metallic silver (Ag^0) and silver oxides (Ag_xO) undergo during aging, and the implications for their antimicrobial activity and cytotoxicity.

2. Materials and Methods

2.1. Stent Production and Functionalization

Braided fibrous polyester (PES) stents comprising monofilaments of PES 0.27 mm in diameter and a mandrel 6 mm in diameter with 35°of braiding angle were produced according to the methodology described by Rebelo and co-workers [6]. Both stent and Ag impurities were removed in a petroleum ether ultrasonic bath for 1 h, followed by an argon (Ar) plasma etching during 5 min. The cleaning etching was performed using a pulsed DC power supply with the following specifications: 0.4 A, 200 kHz, 1536 ns of reverse time, a current density of 0.5 mA cm^{-2} within an 80 sccm Ar atmosphere. Ag^0 and Ag$_x$O coatings were deposited by non-reactive and reactive pulsed DC magnetron sputtering, respectively. The deposition was performed as described by Rebelo and co-workers [21]. In brief, coatings were deposited from Ag target (200 × 100 mm^2—purity of 99.99%), varying the oxygen flow. Stents were placed in a substrate holder 70 mm away from the target with a constant rotation velocity of 7 rpm. Samples of silicon and stainless steel were placed along the stents, in order to easily characterize the coating, namely by X-ray diffraction (XRD) analysis. The presence of oxygen was mandatory for the deposition of reactive mode to obtain Ag$_x$O coatings, and its optimization is described elsewhere [20]. The stents were aged for a period of 3 months at room temperature in a desiccator, protected from light. To further analyze the nanostructure of the coated stent, an Ar$^+$ ionic erosion was performed according to the conditions described by Altstetter and Tortorelli, using a beam of 15 keV of Ar$^+$ [22].

2.2. Coatings Characterization

To determine the coating binding status, coated silicon samples were analyzed by X-ray photoelectron spectroscopy (XPS) (Kratos Analytical, Manchester, UK). The Kratos AXIS Ultra HSA equipment was used with a monochromatic Al Kα X-ray source (15 keV, 90 W) in fixed analyzer transmission mode (FAT) mode, encompassing a pass energy of 40 eV and a pass of 0.1 eV for regions of interest (ROI). A pressure lower than 1×10^{-6} Pa and a charge neutralization system were applied. Experimental data were collected and analyzed using VISION software (Vision Manager software v. 2.2.10 revision 5) and CasaXPS software (Version 2.3.15), respectively. Carbon peak reference (285 eV) was used to correct the effect of electric charge.

The morphology of stents coated with Ag^0 and Ag$_x$O, were evaluated by scanning electron microscopy (SEM) analysis with EDAX (FEI Company, Hillsboro, OR, USA). Nova nano-SEM200 equipment, prior to and after mechanical tests. XRD analysis, in a PANalytical X'Pert PRO MPD system using Cu Kα radiation (45 kV and 40 mA) with a parallel beam configuration (Malvern Panalytical Ltd., Malvern, UK), was undertaken with the purpose of understanding the structure and phase distribution of the coatings. The analysis was performed in grazing incidence mode with an angle of incidence of 5°, and the grain size was determined by the Scherrer equation (Equation (1)).

$$T = \frac{K\lambda}{\beta \cos \theta},\tag{1}$$

where, *T* corresponds to the mean size of the ordered (crystalline) domains (nm), *K* to dimensionless shape factor, λ to the X-ray wavelength (nm), β to the half the maximum intensity (FWHM) (rad), and θ to the Bragg angle (°).

The modified Auger parameter was estimated using Equation (2) [23].

$$\alpha' = BE(\text{Ag } 3d_{5/2}) + KE(\text{AgM}_4\text{N}_{45}\text{N}_{45}),\tag{2}$$

where, $BE(\text{Ag } 3d_{5/2})$ corresponds to the maximum binding energy (*BE*) of Ag $3d_{5/2}$ peak in the Ag $3d$ spectrum and $KE(\text{AgM}_4\text{N}_{45}\text{N}_{45})$ to the maximum kinetic energy (*KE*) of the AgM$_4$N$_{45}$N$_{45}$ peak in the AgMNN spectrum (strongest transitions between electrons whose orbitals are closest together).

2.3. Mechanical Properties

The mechanical properties before and after stent functionalization were evaluated. Cover factor indicates the amount of fiber deposited on the mandrel surface, depending on fabrication parameters, and it is a good indicator of stent structural uniformity. Porosity is also an important parameter and it should range between 70% and 80% in order to avoid stent collapse [24]. Cover factor and porosity can be calculated using Equations (3) and (4) [6].

$$Cover\ factor = 1 - \left(\frac{W_y N_c}{4\pi R \cos \alpha} \right)^2, \tag{3}$$

$$Porosity = 1 - Cover\ factor, \tag{4}$$

where, W_y is monofilament width (mm), N_c corresponds to the number of bobbins, R to mandrel radius (mm), and α is braiding angle (rad). Stents were of 40 mm in length and 6 mm in radial diameter. Radial and longitudinal compression were tested in a universal testing machine. In all tests, for each kind of sample (PES stents, silver-coated stent and silver oxide-coated stent) 15 samples were used and the necessary force for the compression was measured [6,25]. Radial compression plays an important role in stent behavior, since insufficient radial force can lead to revision surgeries. For radial compression tests, stents were compressed until 25% of their initial diameter.

Stents were compressed by 15% of their original diameter (6 mm) during longitudinal compression, and longitudinal force was estimated.

We bent 40 mm-length stents until their extremities were separated by 2 cm and diameter was measured at midpoint of the bending section, according to Kim and colleagues [26]. The percentage of unchanged diameter, in the bending section, was calculated through Equation (5) [6].

$$Unchanged\ diameter = \left(\frac{D_b}{D_i} \right) \times 100, \tag{5}$$

where D_b is stent diameter in bent condition (mm) and D_i the initial stent diameter (mm).

2.4. Antibacterial and Cytotoxicity Assessment

All aged stents were sterilized at 121 °C during 15 min in an autoclave, prior to biological assays.

A clinical isolate *S. epidermidis* (IE 186) was used to assess the bactericidal properties of the aged stents, by performing an adaptation of Standard Japanese Industrial Standard (JIS) Z 2801 [27]. Bacterium was cultured in tryptic soy broth (TSB), during 24 h at 37 °C and 120 rpm. The initial bacterium concentration used was 1×10^6 colony forming units (CFU) mL^{-1}. Aged stents were immersed in 3 mL of TSB with bacterium suspension and incubated for 24 h at 37 °C and 120 rpm. Afterwards, the stents were transferred into 5 mL of a sodium chloride 0.85% (*w/v*) solution with 1% (*v/v*) of polysorbate 80. Samples were vortexed 5 times for 5 s each, to detach bacteria from the stent surface. Both detachment buffer and TSB bacterium suspensions were submitted to serial dilution and were plated in tryptic soy agar (TSA), and incubated at 37 °C for 24 h. Thereafter, the CFU were estimated. All assays were run in triplicate.

For SEM analysis, aged stents were incubated in the same conditions. Then, the bacterium at the stent's surface were fixated according to the protocol described by Padrão and co-workers [28]. Briefly, stents were carefully immersed in a solution of 2.5% (*v/v*) glutaraldehyde in phosphate-buffered saline (PBS) for 1 h. Afterwards, stents were mildly rinsed with distilled water and dehydrated using ethanol solutions with increasing concentration (55%, 70%, 80%, 90%, 95%, 100% (*v/v*)), for 30 min per solution. The remaining ethanol was left to evaporate, and the samples were gold sputtered.

Cytotoxicity evaluation assays were performed using an adaptation of International Organization for Standardization (ISO) 10993-5 and CellTiter 96® AQueous One Solution Cell Proliferation protocols [29]. Stainless steel was coated with Ag^0 and Ag$_x$O, and aged in the same conditions

as the coated stents. These samples were used in cytotoxicity tests due to their less complex geometry when compared to braided stents.

Fibroblast 3T3 (CCl-163) acquired from the American Type Cell Collection (ATCC) (Manassas, VA, USA) were cultured in Dulbecco Modified Eagle's Medium (DMEM) containing 1% (*v/v*) of penicillin streptomycin (PS) and 10% (*v/v*) of fetal bovine serum (FBS) until obtaining 80% of confluence. After cells detachment, 50 μL of cell suspension containing 1×10^5 cells mL^{-1} were added to each sample in a 96 well plate and incubated for 24 h, at 37 °C in a humidified atmosphere containing 5% (*v/v*) of carbon dioxide. 50 μL of the medium in contact with the samples were removed from each well and added to a 96-well plate with cells, incubated in the same conditions for 24 h. After the incubation, 20 μL of 3-(4,5-dimethylthiazol-2-yl)-5-(3-carboxymethoxyphenyl)-2-(4-sulfophenyl)-2H-tetrazolium (MTS) was added, in the dark, to each well of the 96-well plate. The plate was incubated in the same conditions for 1 h and the absorbance of the resulting solution was measured at 490 nm.

Cellular viability was measure taking in account the ratio of the difference between cells grown in the control (samples without coating considered 100% viability) and coated samples over the control growth (Equation (6)). Assays were run in triplicate.

$$Cell\ viability\ (\%) = \left(\frac{Sample}{Control}\right) \times 100, \tag{6}$$

2.5. Statistical Analysis

One-way analysis of variance (ANOVA) with Tukey's multiple comparisons post-test was used (GraphPad Prism 6). All tests were performed with a confidence level of 95%.

## 3. Results and Discussion

3.1. Physicochemical Characterization

Figure 1 shows the braided uncoated PES stents (Figure 1a), the stent coated with Ag^0 (Figure 1b), the stent coated with Ag$_x$O (Figure 1c), as well as the aged Ag^0 (Figure 1d) and aged Ag$_x$O (Figure 1e). The thin film of the coatings was generated by physical vapor deposition using direct current (DC) magnetron sputtering. It is a fast and user-friendly deposition method that does not require high temperature, essential to maintain the integrity of the PES stents. Furthermore, it allows a controllable film thickness and is environmentally friendly [30]. No red coloration of the uncoated PES fibers can be observed in both coated stents (Ag^0 and Ag$_x$O). The aged Ag^0 stent is darker and more yellowish due to the metal silver oxidation and the presence or carbonates. The aged Ag$_x$O stent exhibits a lighter brown color, probably, also due to the formation of silver carbonate that by contrast with the black coloration of silver oxide is known to have a white to yellow coloration.
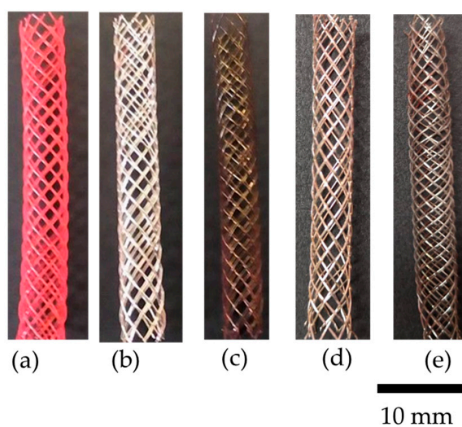
Figure 1. Braided polyester (PES) stents; (**a**) uncoated; (**b**) Ag^0 coated and (**c**) Ag$_x$O coated, (**d**) aged Ag^0 coated and (**e**) aged Ag$_x$O coated.

XPS analysis of Ag and Ag$_x$O coatings was carried out before (aged) and after a surface Ar$^+$ ionic erosion. The high-resolution spectra of Ag core-level, Auger peak, the C 1s peak, and the O 1s peak were examined with the intention of evaluating the chemical state and energy of the coating surface as previously performed [21]. Prior to erosion, both O 1s and C 1s envelopes contained shoulders that were deconvoluted indicating that multiple chemical states of carbon and oxygen were present on the coating surfaces. The core level photoemission spectra of C 1s obtained for Ag^0 coated surface was best fitted (full width at half maximum (FWHM) 1.2 eV) by means of four components (Figure 2). The carbon peak at the lowest BE centered at 285 eV is assigned to adventitious carbon (C–C and/or C–H), while the second, located at 286.2 eV, is associated with C–OH bonding. The peak located at 288 eV is mainly ascribed either to silver carbonates or bicarbonates due to the interactions of Ag^0 with the outer atmosphere. Previous XPS studies of Ag^0, AgO and Ag$_2$O have shown that CO$_2$ present in the air could be responsible for the formation of Ag$_2$CO$_3$ layers on these surfaces [31–33]. The higher BE peak at 289.2 corresponds to O–C=O bonding of the carbonate group of Ag$_2$CO$_3$ [34]. High-resolution O 1s spectra depicted in Figure 2 corroborates the presence of Ag carbonate or bicarbonate (531.2 eV) [35]. The presence of stable chemically absorbed molecular oxygen (532.5 eV) and water (534.3 eV) further verifies the interactions of Ag^0 with the outer atmosphere [32,36]. A previous work confirmed through Raman analysis the existence of surface carbonate and surface oxygen species (superoxide oxygen and hydroxyl species) in Ag^0 displaying a similar peak in O 1s [37]. As expected, despite atmospheric interaction, no characteristic AgO and Ag$_2$O ($\approx$529 eV) are observable, since Ag^0 is not oxidized at ambient pressure by atmospheric oxygen [38]. After Ar$^+$ erosion, the Ag^0 surface was etched, removing all surface-contaminating species, revealing the coating original status obtained immediately after sputtering without any traces of C or O species.
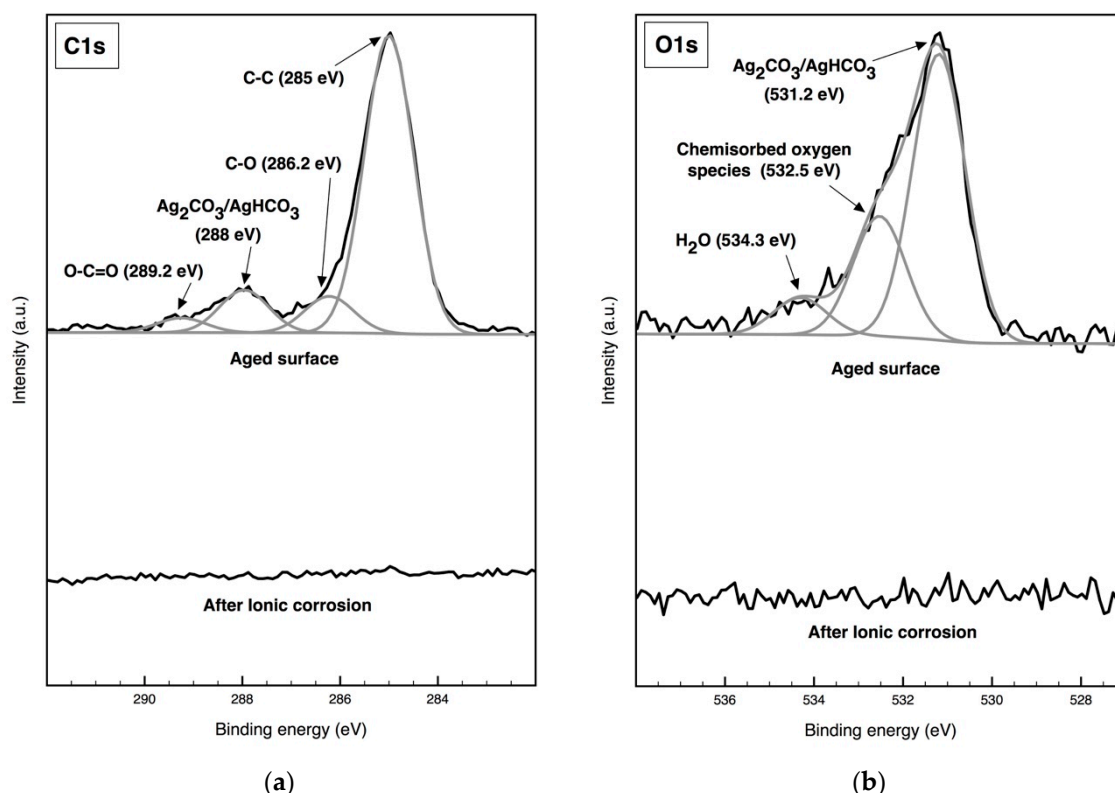
Figure 2. High-resolution X-ray photoelectron spectroscopy (XPS) C 1s (**a**) and O 1s (**b**) spectra for Ag^0 coatings before and after Ar$^+$ ionic erosion.

Figure 3 displays the XPS analysis of Ag$_x$O coatings. The highest BE peak of C 1s spectra is attributed to the functional C–C component (285 eV), followed by Ag carbonate or bicarbonate (288.5 eV), and its carboxyl group (286.5 eV) [32]. The Ag$_x$O O 1s spectra displays the presence of

chemisorbed oxygen (533 eV) and a mixture of Ag_2O and AgO (529.3 eV). The main peak is attributed to Ag carbonate/bicarbonate species (531.4 eV) [32]. After Ar^+ ionic erosion, Ag carbonate/bicarbonate is still present even if in a small quantity (531.3 eV) and it is denoted as a shift from 529.3 to 529.7 eV of the peak attributed to the Ag_xO species. This minor shift can be ascribed to a difference in the ratio of the Ag_2O/AgO species. Since the BE is lower in the aged coating, it may be attributed to higher concentration of AgO in the mixture [39,40].
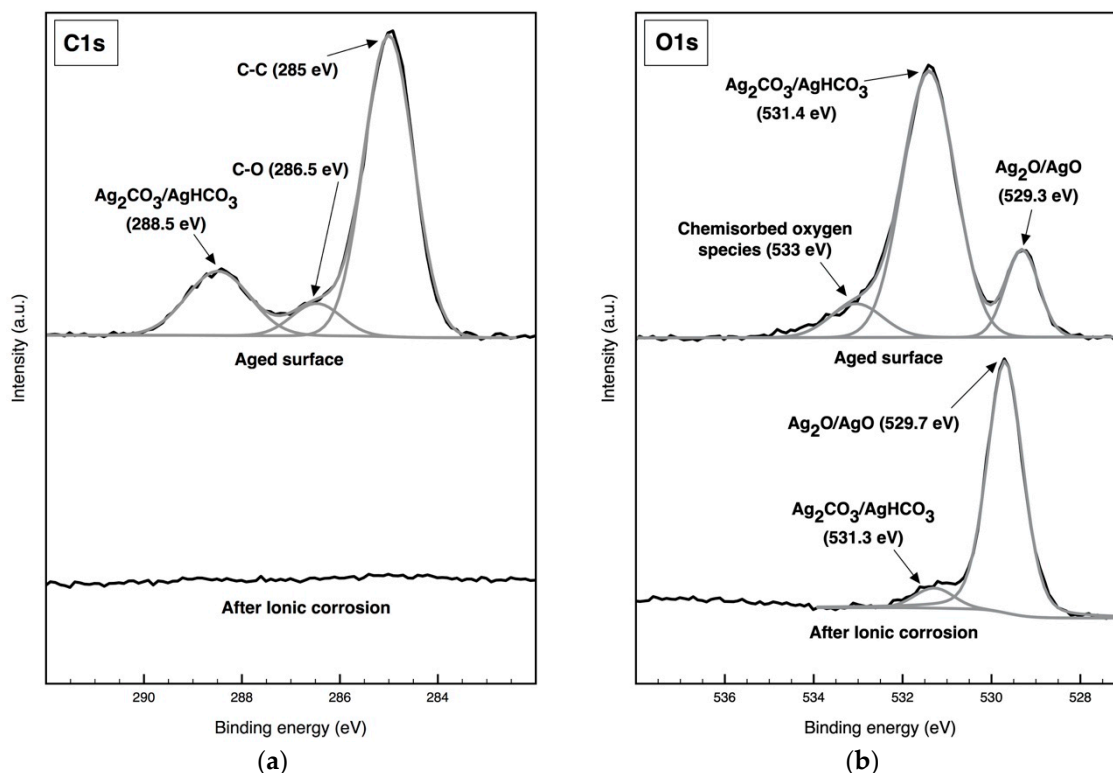
Figure 3. High-resolution XPS C 1*s* (**a**) and O 1*s* (**b**) spectra for Ag_xO coatings before and after Ar^+ ionic erosion.

XPS analysis of silver and silver oxides is quite complex, due to the proximity of binding energies that are reported with a low dispersion of values or even superposition, and the Auger parameter (*AP*) was also considered. *AP* is used to identify the *BE* for oxidation, once *AP* does not depend on the sample charge shift, avoiding charge correction. Furthermore, the peaks of *AP* present larger chemical shifts than photoelectron peaks [40]. The main disadvantage of *AP* is that it cannot distinguish Ag(I) form others oxidation states [40]. Figure 4 shows the spectra of *BE* for Ag 3*d*. As expected, Ag 3*d* spectra display spin orbit components separated by 6 eV [40]. Ag $3d_{3/2}$ and Ag $3d_{5/2}$ binding energies prior and after Ar^+ ionic erosion are centered approximately at 374.9 ± 0.3 eV and 368.7 ± 0.3 eV, respectively. This is in good agreement with the values described for Ag^0 [33,37]. After Ar^+ ionic erosion, a minor shift in the energy binding and kinetic energy can be observed. Ag 3 $d_{3/2}$ and Ag $3d_{5/2}$ peaks in the Ag 3*d* spectra display a negative shift of −0.4 eV, and a peak narrowing after Ar^+ ionic erosion. AgMNN (letters correspond to the principal energy level, or electron shells, associated with the Auger process) spectra also show narrowing of $AgM_4N_{45}N_{45}$ and $AgM_5N_{45}N_{45}$ peaks, and a slight negative shift of $AgM_4N_{45}N_{45}$ after Ar^+ ionic erosion (−0.5 eV). These slight differences observed in all spectra may be associated with the elimination of the silver carbonate and bicarbonate species. The Ag $3d_{5/2}$ peak is located at 368.7 ± 0.3 eV. This fact, along with AP (726.2 ± 0.1 eV) (Table 1), is in good agreement with the reported values for Ag^0 [41,42].
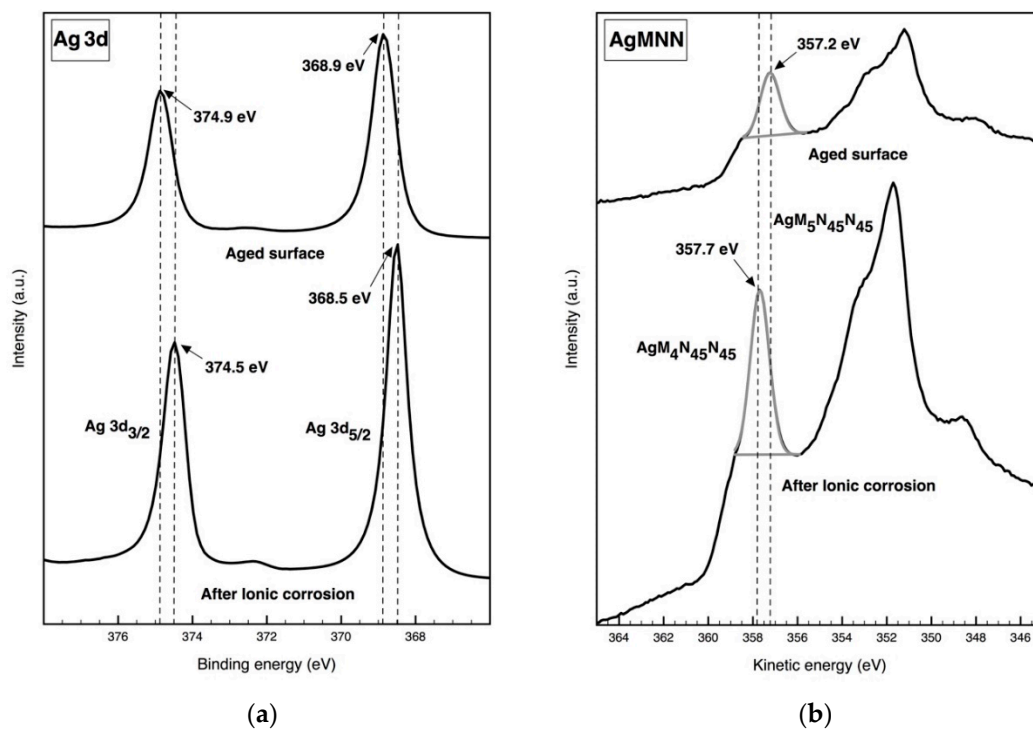
Figure 4. High-resolution XPS Ag 3*d* (**a**) and AgMNN (**b**) spectra for aged Ag^0 coatings and after Ar^+ ionic erosion.

Table 1. Relative chemical composition (at.%), atomic ratio and Auger parameter of aged Ag^0 and Ag_xO Ar^+ before and after Ar^+ ionic erosion. ND: Not detected.

|	Aged Surface						Ar^+ Ionic Erosion					
	at.%				Atomic Ratio	Auger	at.%				Atomic Ratio	Auger
Ag Coating	C 1*s*	O 1*s*	S	Ag 3*d*	Ag/O	α'	C 1*s*	O 1*s*	S	Ag 3*d*	Ag/O	α'
Ag	34.82	9.86	0.61	54.71	-	726.1	0.39	ND	ND	99.61	-	726.2
Ag_xO	40.04	29.93	2.62	27.42	0.92	723.5	0.91	27.1	ND	71.99	2.66	724.6

High-resolution Ag 3*d* spectra of the Ag_xO coatings spectra do not denote any shift; however, both Ag 3*d*$_{3/2}$ and Ag 3*d*$_{5/2}$ became narrower after Ar^+ ionic erosion (Figure 5a). As observed previously in Ag^0 Ag 3*d* spectra (Figure 4), peak narrowing may be due to the etching of silver carbonate/bicarbonate. However, the AgMNN spectra (Figure 5b) exhibit a significant shift after ionic Ar^+ erosion (−1.1 eV). This shift is in agreement with that observed in Figure 3, regarding the *BE* shift of −0.4 eV. These shifts along with the *AP* value denote a distinct silver oxygen species ratio prior to and after Ar^+ ionic erosion coatings [43].

XRD analysis was performed in order to obtain information about coating structure. Figure 6 shows XRD diffraction patterns for aged Ag^0 and Ag_xO coatings. Crystalline phases were identified as Ag (International Centre for Diffraction Data (ICDD) card n° 00-004-0783) and AgO (ICDD card n° 00-043-1038). Regarding aged Ag^0 coating, XRD analysis, reveals that it crystallizes in a face-centered cubic (fcc-Ag) crystal structure with random oriented crystallites and a grain size of 78.5 nm, calculated for (111) peak, while aged Ag_xO coating was identified as a monoclinic phase with a grain size of 35.9 nm for (−111) peak. These results are in agreement with the expected structures for Ag^0 and Ag_2O/AgO mixture [44].
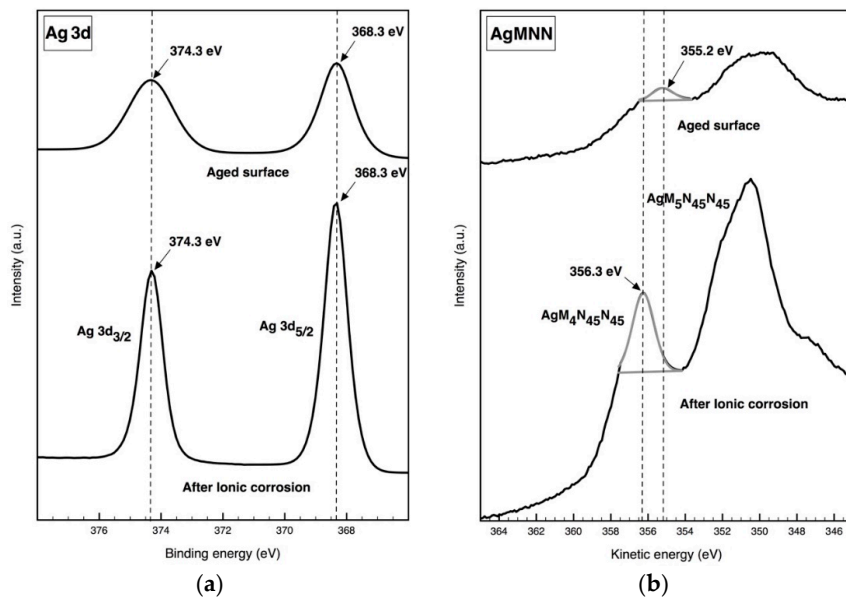
Figure 5. High-resolution XPS Ag 3*d* (**a**) and AgMNN (**b**) spectra for aged Ag$_x$O coatings before and after Ar$^+$ ionic erosion.
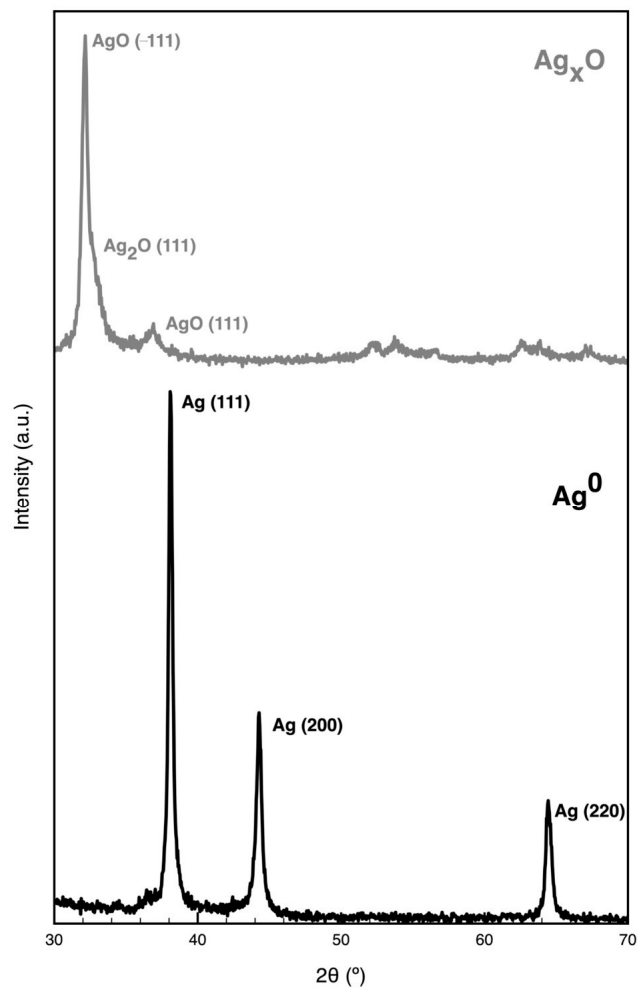
**Figure 6.** X-ray diffraction (XRD) patterns of the aged Ag^0 and Ag$_x$O coatings.

SEM analysis on coated stents, presented in Figure 7, shows a homogenous coating in both samples with a more columnar and porous structure in Ag_xO coating, when compared with Ag^0, due to the introduction of oxygen, which minimizes the porosity and leads to the formation of more compact films, with lower column size, as evaluated in previous work [21]. The aged coated stents were subjected to mechanical forces and SEM was used to analyze coating integrity. From the analysis of Figure 7 it is possible to observe differences in the morphology of silver-coated stents after the mechanical tests. A rearrangement of silver columns is noticeable, due to the ductile properties of the coating that may accumulate the tensions to which it is subjected and deform without being disrupted. However, no other considerable changes, like delamination, were visible in silver and silver oxide coatings, after the mechanical tests.
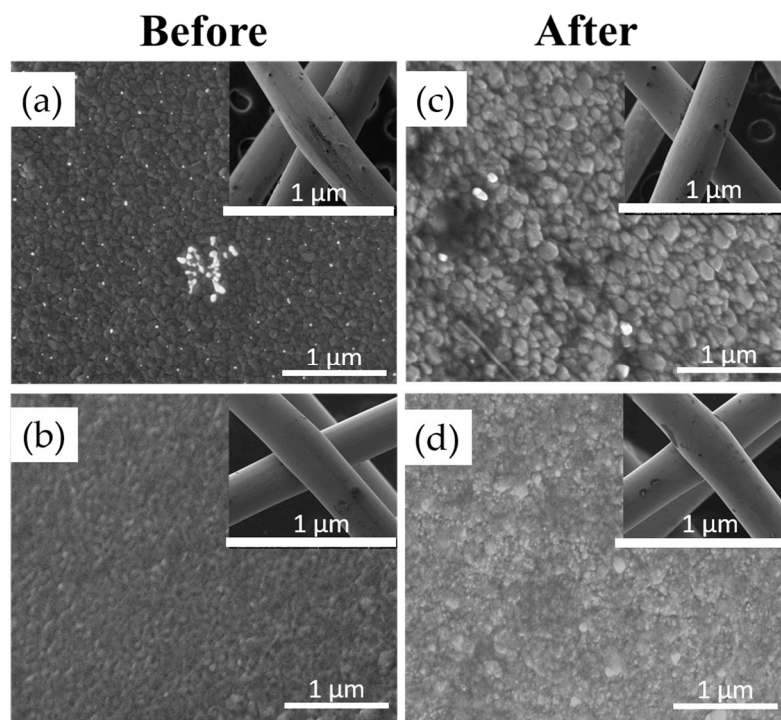
Figure 7. Scanning electron microscopy (SEM) micrographs of aged Ag^0- and aged Ag_xO-coated stents before (**a**) and (**b**) and after (**c**) and (**d**) mechanical tests, respectively.

Figure 8 also shows the mechanical behavior of uncoated and coated PES stents, upon longitudinal and radial compression. As previously observed in the mechanical characterization of these stents by our group, when the compressions were applied stents underwent a structural deformation modifying their diameter and braiding angle [6]. Mechanical analysis of coated surfaces is not linear, due to the complexity of atom interactions between the substrate and the thin-film coating [45]. All samples presented a linear behavior under compression, which indicates that for the required extension, stents remained in the elastic domain with no permanent alteration in the braided structure. When comparing polyester uncoated and coated stents in longitudinal compression, it is clear that the coating is the main determinant influencing the mechanical behavior. Stiffness of the uncoated stent 0.02 N mm^{-1} is similar to the aged Ag^0 stent and to the aged Ag_xO stent (0.05 and 0.03 N mm^{-1}, respectively). Higher stiffness implies the application of a higher force to perform the same elongation [46]. Regarding radial compression, the materials' influence is not so clear, as the braided structure seems to play a key role in the process, due to the fact that the contact area between the stent and the applied force is much higher. Aged Ag^0-coated stent presented a lower radial stiffness (0.36 N mm^{-1}) whereas the aged Ag_xO-coated stent displayed a higher radial stiffness (0.90 N mm^{-1}), when compared to the uncoated PES stent (0.55 N mm^{-1}). Ag coatings are considered lubricants,

thus, and considering the structure possess the main contribution for the radial compression behavior, the incorporation of Ag coatings can lead to a slippage between the monofilaments which may explain the lower force observed for Ag^0-coated stents [47,48]. It is harder to draw a hypothesis for the 1.6-fold increase of the radial compression exhibited by the Ag_xO, due to the lack of information in the literature. However, there is a report of a hardness increase when Ag oxides are present, due to changes in the roughness of the material [49].
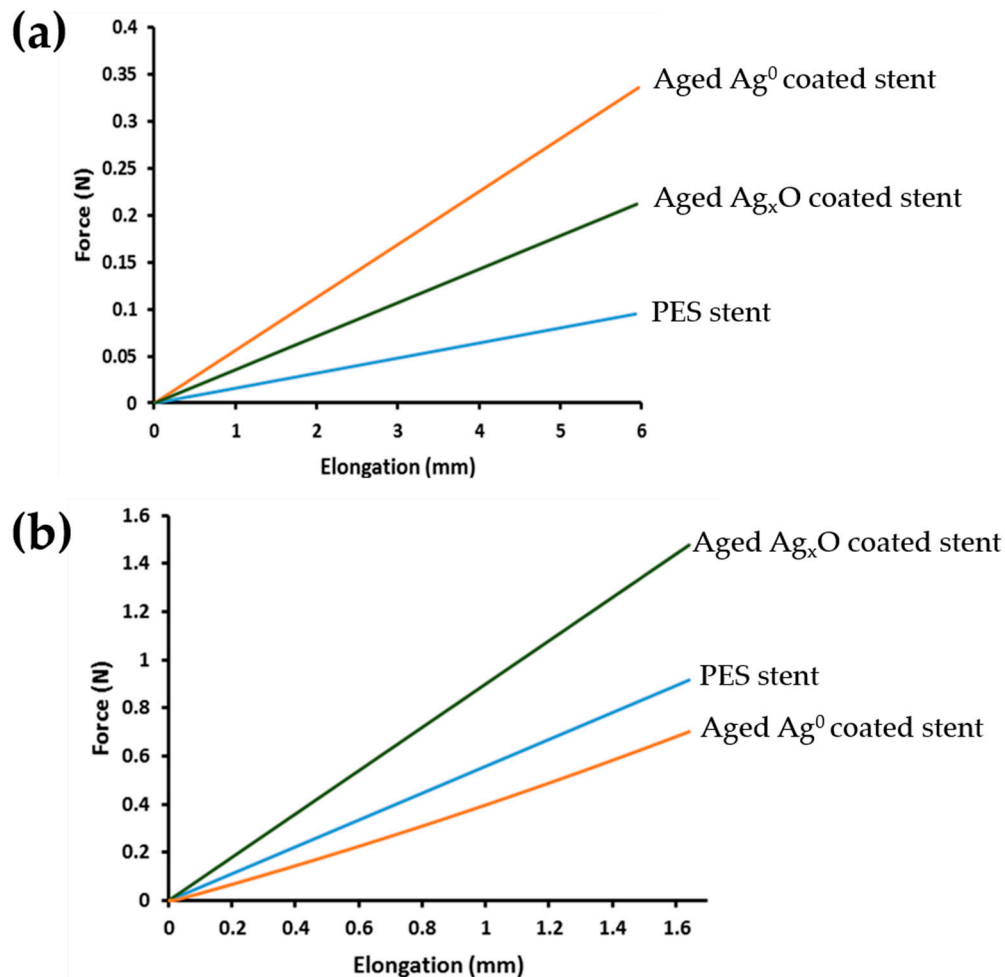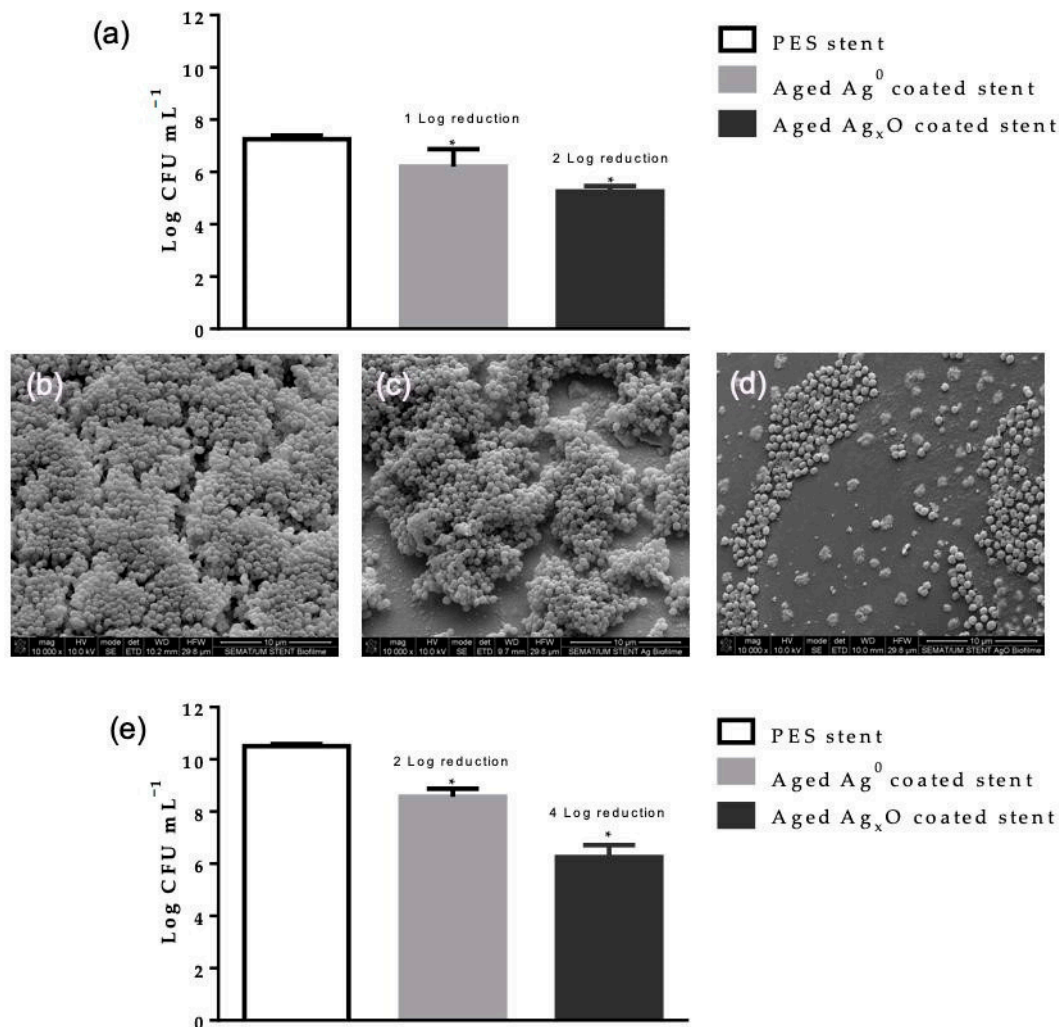

Figure 8. Aged Ag^0- and aged Ag_xO-coated stents behavior displayed between force and elongation for longitudinal (**a**) and radial (**b**) compression.

3.2. Biological Performance

S. epidermidis is one of the most ubiquitous human skin colonizer bacteria [50], described as an important nosocomial pathogen, responsible for numerous infections of immunocompromised patients carrying medical devices [51], particularly due to its biofilm forming capabilities [52]. Figure 8 comprises the antimicrobial efficacy of the aged coated stent's surface and within its vicinity. Figure 8a shows the bacterium cell concentration at the tested PES stent's surface. It denotes a Log 1 and a Log 2 reduction at the surface of aged Ag^0 and aged Ag_xO, respectively (Figure 9a). These results are corroborated by SEM images, which confirm *S. epidermidis* has an extensive biofilm formation on the stent's surface. The aged Ag^0-coated stent exhibited an apparent lower bacterium concentration than the PES stent, and the aged Ag_xO stent shows not only a visual clear reduction in the bacterium concentration but also displays the presence of unviable bacteria (Figure 9b–d). Ag^0 displayed approximately a Log 2 reduction and Ag_xO exhibited an effective antimicrobial action (Log 4 reduction) (Figure 9e). This indicates a more potent vicinity action than at the stent surface. The higher susceptibility of several planktonic bacteria

to the action of silver has already been reported in the literature. Planktonic *Pseudomonas aeruginosa*, *Staphylococcus aureus* and *Enterobacter cloacae* were promptly and extensively killed by silver bactericidal action whereas their biofilm counterparts exhibited higher resistance, by exhibiting less cell death and by delaying the silver bactericidal activity (in approximately 70 h) [53], underscoring the higher virulence of biofilms.

Figure 9. PES stents, control (solely PES), aged Ag^0-coated and aged Ag_xO stents' efficacy against *S. epidermidis*. (**a**) Bacteria concentration on the stent's surface. SEM micrograph of *S. epidermidis* biofilm on the surface of: (**b**) PES stent, (**c**) aged Ag^0 and (**d**) aged Ag_xO. (**e**) Bacteria concentration in the medium incubated with the stents. Significant differences between the aged coated and the control are highlighted with a * ($p < 0.05$).

Ag-based coatings using several deposition techniques has been extensively studied and good results in terms of antibacterial efficiency are commonly observed [54]. Despite its widespread use, the exact mechanism of actuation of the Ag as an antimicrobial agent is still not completely understood. Moreover, the bactericidal efficacy of each Ag species does not generate a clear consensus. In this work, the coatings Ag concentration is very similar (Ag^0 coating: 0.17 ± 0.01 mg L^{-1} and Ag_xO coating: 0.16 ± 0.01 mg L^{-1}) [21]. Therefore the observed 2-fold difference may be associated with a suggested *modus operandi* of Ag antibacterial properties, the release of Ag^+ [55]. Ag^0 firstly needs to be oxidized to release Ag^+, which is a slow process [56] whereas, Ag^+ elution from Ag_xO is a fast process (up to 0.07 ppm min^{-1}) [57]. Ag^+ disrupts the activity of enzymes containing L-cysteine residue, and it was demonstrated that Ag^+ mediated the generation of reactive oxygen species (ROS), particularly of

superoxide radical ($O_2{}^-$) [58]. ROS are known to induce cell death through several mechanisms, DNA being one of its critical targets [59]. Extensive mutagenesis irrevocably causes bacterial cell death [60], moreover ROS are soluble species, which may explain the observed higher Log reduction in the medium in comparison with the stent surface. Previous studies report that Ag^0 thin films display less Ag ionization [20,21], thus aged Ag_xO coating may generate a higher Ag^+, which may explain the 2-fold higher antimicrobial activity. Interestingly, aging may have promoted the higher Log reduction in the medium, since both aged coatings exhibited the presence of Ag carbonate/bicarbonate on the stents' surface, as observed in XPS. Considering that, Buckley and colleagues observed a Log 3 reduction of *S. aureus* by $AgCO_3$ [61], a similar action may have occurred with the aged stents. Finally, the higher resistance of the biofilm cells present on the surface of the stents may be correlated to the mitigation of the ROS by the extracellular polymeric substances (EPS) [62]. Figure 10 exhibits a diagram of the hypothesized bactericidal activity of the coated stents.
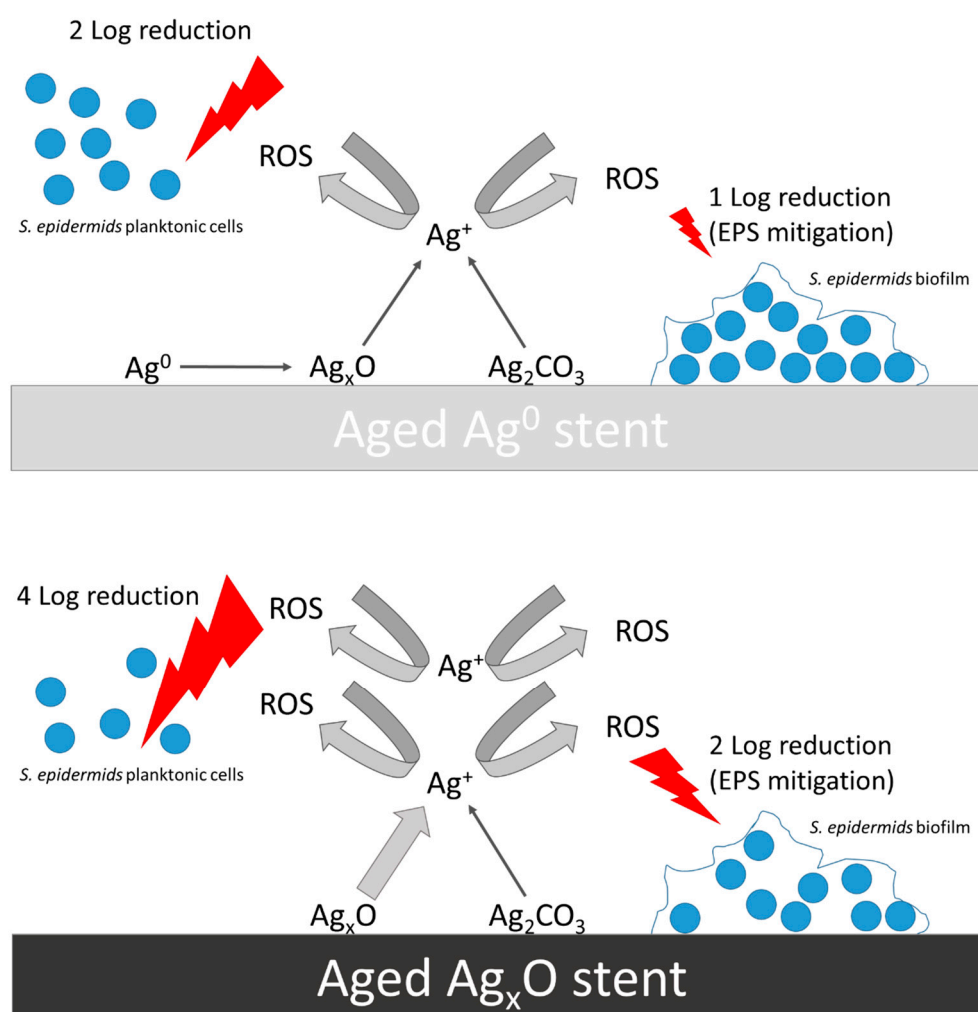
Figure 10. Diagram of the proposed bactericidal activity of the aged coated stents.

Cytotoxicity evaluation assays depict a cellular viability superior to 70% (Figure 11), determined as a threshold for cytotoxicity [28]. ROS usually display a lower toxicity for the animal cells in comparison to bacteria, since animal cells possess a plethora of ROS damage mitigation mechanisms [63]. Thus, according to cytotoxicity results, it is viable to insert coated stents in the human body and use antibacterial braided material.
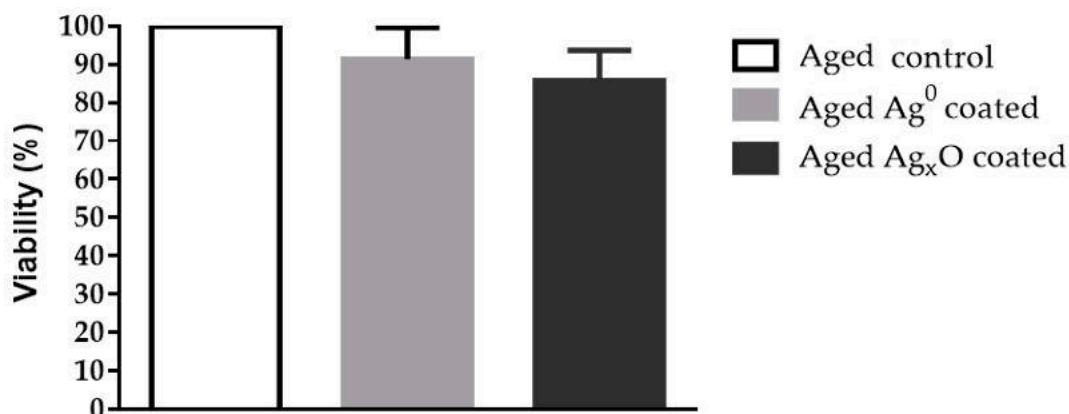
Figure 11. Fibroblast culture viability percentages.

4. Conclusions

Commercial application Ag^0 and Ag_xO thin-film PES stents are not expected to be implanted in an atherosclerosis patient immediately after their production. Therefore, an aging period is paramount to provide an insight on their performance in terms of surface properties, mechanical behavior, antimicrobial activity and biocompatibility. XPS showed that both aged Ag^0 and Ag_xO stent surfaces possessed Ag carbonate or bicarbonate, chemically absorbed molecular oxygen, and water, due their reactivity with the atmosphere. Aged Ag^0 stents exhibited lower antibacterial activity at their surface and in the vicinity than Ag_xO and no relevant cytotoxicity. More importantly, aged Ag_xO stents showed a mild bactericidal effect on the surface and an effective antibacterial activity in its vicinity, with tolerable cytotoxicity towards fibroblasts. These conclusions are important to highlight the bactericidal effectiveness of the surfaces of Ag^0 and Ag_xO thin films despite the presence of Ag carbonate or bicarbonate species. In fact, once the stents are implanted within the human body, the carbon dioxide present in the blood flow can promptly generate Ag carbonate or bicarbonate species at the surface of the coated stents. This work provides a first indication that the presence of these species will not hinder the bactericidal effectiveness nor increase the cytotoxicity, further corroborating the adequacy of these indwelling devices.

Author Contributions: R.R. performed the main analysis and data collection. J.P. wrote the manuscript and performed data interpretation. M.M.F. performed data interpretation, M.H. performed and interpreted the antimicrobial analysis, S.C. and A.Z. performed the XPS deconvolutions, supervise all works and finalize the manuscript. R.F. supervised all works and finalize the manuscript. All authors have read and agreed to the published version of the manuscript.

Conflicts of Interest: The authors declare no conflict of interest.

References

1. Wilkins, E.; Wilson, L.; Wickramasinghe, K.; Bhatnagar, P.; Leal, J.; Luengo-Fernandez, R.; Burns, R.; Rayner, M.; Townsend, N. *European Cardiovascular Disease Statistics 2017*; European Heart Network: Brussel, Belgium, 2017.
2. Tabaei, S.; Tabaee, S.S. DNA methylation abnormalities in atherosclerosis. *Artif. Cells Nanomed. Biotechnol.* **2019**, *47*, 2031–2041. [CrossRef] [PubMed]
3. Byrne, R.A.; Joner, M.; Alfonso, F.; Kastrati, A. Drug-coated balloon therapy in coronary and peripheral artery disease. *Nat. Rev. Cardiol.* **2013**, *11*, 13–23. [CrossRef] [PubMed]

4.   Driver, M. Coatings for cardiovascular devices: Coronary stents. In *Coatings for Biomedical Applications*; Driver, M., Ed.; Woodhead Publishing Series in Biomaterials; Woodhead Publishing: Cambridge, UK, 2012; pp. 223–250. ISBN 978-1-84569-568-2.

5.   Rebelo, R.; Fangueiro, R.; Carvalho, S.; Henriques, M.; Rana, S. Methods of incorporation antimicrobial agents in stents. *Int. J. Eng. Sci. Innov. Technol.* **2014**, *3*, 1–17.

6.   Rebelo, R.; Vila, N.; Fangueiro, R.; Carvalho, S.; Rana, S. Influence of design parameters on the mechanical behavior and porosity of braided fibrous stents. *Mater. Des.* **2015**, *86*, 237–247. [CrossRef]

7.   Irsale, S.; Adanur, S. Design and characterization of polymeric stents. *J. Ind. Text.* **2006**, *35*, 189–200. [CrossRef]

8.   Dyet, J.F.; Watts, W.G.; Ettles, D.F.; Nicholson, A.A. Mechanical properties of metallic stents: How do these properties influence the choice of stent for specific lesions? *Cardiovasc. Intervent. Radiol.* **2000**, *23*, 47–54. [CrossRef]

9.   Panthier, F.; Warein, E.; Cochennec, F.; Desgranges, P.; Touma, J. Early onset of acute lower limb drug-eluting stent infection. *Ann. Vasc. Surg.* **2019**, *61*, 471.e3–471.e7. [CrossRef]

10.   Azeredo, J.; Azevedo, N.F.; Briandet, R.; Cerca, N.; Coenye, T.; Costa, A.R.; Desvaux, M.; Di Bonaventura, G.; Hébraud, M.; Jaglic, Z.; et al. Critical review on biofilm methods. *Crit. Rev. Microbiol.* **2017**, *43*, 313–351. [CrossRef]

11.   Høiby, N.; Bjarnsholt, T.; Moser, C.; Bassi, G.L.; Coenye, T.; Donelli, G.; Hall-Stoodley, L.; Holá, V.; Imbert, C.; Kirketerp-Møller, K.; et al. ESCMID* guideline for the diagnosis and treatment of biofilm infections 2014. *Clin. Microbiol. Infect.* **2015**, *21*, S1–S25. [CrossRef]

12.   Thukkaram, M.; Cools, P.; Nikiforov, A.; Rigole, P.; Coenye, T.; Van Der Voort, P.; Du Laing, G.; Vercruysse, C.; Declercq, H.; Morent, R.; et al. Antibacterial activity of a porous silver doped TiO_2 coating on titanium substrates synthesized by plasma electrolytic oxidation. *Appl. Surf. Sci.* **2020**, *500*, 144235. [CrossRef]

13.   Mani, G.; Feldman, M.D.; Patel, D.; Agrawal, C.M. Coronary stents: A materials perspective. *Biomaterials* **2007**, *28*, 1689–1710. [CrossRef] [PubMed]

14.   Freitas, A.F.D.P.; de Araujo, M.D.; Zu, W.W.; Fangueiro, R.M.E. Development of weft-knitted and braided polypropylene stents for arterial implant. *J. Text. Inst.* **2010**, *101*, 1027–1034. [CrossRef]

15.   Simard, T.; Hibbert, B.; Ramirez, F.D.; Froeschl, M.; Chen, Y.-X.; O'Brien, E.R. The evolution of coronary stents: A brief review. *Can. J. Cardiol.* **2014**, *30*, 35–45. [CrossRef] [PubMed]

16.   Roy, A.; Joshi, M.; Butola, B.S.; Ghosh, S. Evaluation of biological and cytocompatible properties in nano silver-clay based polyethylene nanocomposites. *J. Hazard. Mater.* **2020**, *384*, 121309. [CrossRef] [PubMed]

17.   Mosayyebi, A.; Manes, C.; Carugo, D.; Somani, B.K. Advances in ureteral stent design and materials. *Curr. Urol. Rep.* **2018**, *19*, 35. [CrossRef]

18.   Ramstedt, M.; Ribeiro, I.A.C.; Bujdakova, H.; Mergulhão, F.J.M.; Jordao, L.; Thomsen, P.; Alm, M.; Burmølle, M.; Vladkova, T.; Can, F.; et al. Evaluating efficacy of antimicrobial and antifouling materials for urinary tract medical devices: Challenges and recommendations. *Macromol. Biosci.* **2019**, *19*, 1800384. [CrossRef]

19.   Kędziora, A.; Speruda, M.; Krzyżewska, E.; Rybka, J.; Łukowiak, A.; Bugla-Płoskońska, G. Similarities and differences between silver ions and silver in nanoforms as antibacterial agents. *Int. J. Mol. Sci.* **2018**, *19*, 444. [CrossRef]

20.   Rebelo, R.; Manninen, N.K.; Fialho, L.; Henriques, M.; Carvalho, S. Morphology and oxygen incorporation effect on antimicrobial activity of silver thin films. *Appl. Surf. Sci.* **2016**, *371*, 1–8. [CrossRef]

21.   Rebelo, R.; Calderon, S.V.; Fangueiro, R.; Henriques, M.; Carvalho, S. Influence of oxygen content on the antibacterial effect of Ag-O coatings deposited by magnetron sputtering. *Surf. Coat. Technol.* **2016**, *305*, 1–10. [CrossRef]

22.   Altstetter, C.J.; Tortorelli, P.F. Argon ion surface erosion of niobium. *J. Nucl. Mater.* **1976**, *63*, 235–240. [CrossRef]

23.   Zanna, S.; Saulou, C.; Mercier-Bonin, M.; Despax, B.; Raynaud, P.; Seyeux, A.; Marcus, P. Ageing of plasma-mediated coatings with embedded silver nanoparticles on stainless steel: An XPS and ToF-SIMS investigation. *Appl. Surf. Sci.* **2010**, *256*, 6499–6505. [CrossRef]

24.   Hoi, Y.; Ionita, C.N.; Tranquebar, R.; Hoffmann, K.R.; Woodward, S.H.; Taulbee, D.B.; Meng, H.; Rudin, S. Flow modification in canine intracranial aneurysm model by an asymmetric stent: Studies using digital subtraction angiography (DSA) and image-based computational fluid dynamics (CFD) analyses. *Proc. SPIE Int. Soc. Opt. Eng.* **2006**, *6143*, 61430J. [PubMed]

25.　Maleckis, K.; Anttila, E.; Aylward, P.; Poulson, W.; Desyatova, A.; MacTaggart, J.; Kamenskiy, A. Nitinol stents in the femoropopliteal artery: A mechanical perspective on material, design, and performance. *Ann. Biomed. Eng.* **2018**, *46*, 684–704. [CrossRef]

26.　Kim, J.H.; Kang, T.J.; Yu, W.-R. Mechanical modeling of self-expandable stent fabricated using braiding technology. *J. Biomech.* **2008**, *41*, 3202–3212. [CrossRef]

27.　*JIS Z 2801:2000—Antimicrobial Products—Test for Antimicrobial Activity and Efficacy*; Japanese Standards Association: Tokyo, Japan, 2000.

28.　Padrão, J.; Gonçalves, S.; Silva, J.P.; Sencadas, V.; Lanceros-Méndez, S.; Pinheiro, A.C.; Vicente, A.A.; Rodrigues, L.R.; Dourado, F. Bacterial cellulose-lactoferrin as an antimicrobial edible packaging. *Food Hydrocoll.* **2016**, *58*, 126–140. [CrossRef]

29.　*ISO 10993-5:2009 Biological Evaluation of Medical Devices—Part 5: Tests for In Vitro Cytotoxicity*; International Organization for Standardization: Geneva, Switzerland, 2009.

30.　Tan, X.-Q.; Liu, J.-Y.; Niu, J.-R.; Liu, J.-Y.; Tian, J.-Y. Recent progress in magnetron sputtering technology used on fabrics. *Materials* **2018**, *11*, 1953. [CrossRef] [PubMed]

31.　Kibis, L.S.; Stadnichenko, A.I.; Pajetnov, E.M.; Koscheev, S.V.; Zaykovskii, V.I.; Boronin, A.I. The investigation of oxidized silver nanoparticles prepared by thermal evaporation and radio-frequency sputtering of metallic silver under oxygen. *Appl. Surf. Sci.* **2010**, *257*, 404–413. [CrossRef]

32.　Rehren, C.; Muhler, M.; Bao, X.; Schlögl, R.; Ertl, G. The interaction of silver with oxygen. *Z. Phys. Chem.* **1991**, *174*, 11. [CrossRef]

33.　Weaver, J.F.; Hoflund, G.B. Surface characterization study of the thermal decomposition of Ag$_2$O. *Chem. Mater.* **1994**, *6*, 1693–1699. [CrossRef]

34.　Lee, W.H.; Lee, J.G.; Reucroft, P.J. XPS study of carbon fiber surfaces treated by thermal oxidation in a gas mixture of O$_2$/(O$_2$ + N$_2$). *Appl. Surf. Sci.* **2001**, *171*, 136–142. [CrossRef]

35.　Waterhouse, G.I.N.; Bowmaker, G.A.; Metson, J.B. Oxidation of a polycrystalline silver foil by reaction with ozone. *Appl. Surf. Sci.* **2001**, *183*, 191–204. [CrossRef]

36.　Merino, N.A.; Barbero, B.P.; Eloy, P.; Cadús, L.E. La$_{1-x}$CaxCoO$_3$ perovskite-type oxides: Identification of the surface oxygen species by XPS. *Appl. Surf. Sci.* **2006**, *253*, 1489–1493. [CrossRef]

37.　Waterhouse, G.I.N.; Bowmaker, G.A.; Metson, J.B. Interaction of a polycrystalline silver powder with ozone. *Surf. Interface Anal.* **2002**, *33*, 401–409. [CrossRef]

38.　Zemlyanov, D.Y.; Savinova, E.; Scheybal, A.; Doblhofer, K.; Schlögl, R. XPS observation of OH groups incorporated in an Ag(111) electrode. *Surf. Sci.* **1998**, *418*, 441–456. [CrossRef]

39.　Hoflund, G.B.; Hazos, Z.F.; Salaita, G.N. Surface characterization study of Ag, AgO, and Ag$_2$O using X-ray photoelectron spectroscopy and electron energy-loss spectroscopy. *Phys. Rev. B* **2000**, *62*, 11126–11133. [CrossRef]

40.　Ferraria, A.M.; Carapeto, A.P.; do Rego, A.M.B. X-ray photoelectron spectroscopy: Silver salts revisited. *Vacuum* **2012**, *86*, 1988–1991. [CrossRef]

41.　Calderon, V.S.; Galindo, R.E.; Benito, N.; Palacio, C.; Cavaleiro, A.; Carvalho, S. Ag+release inhibition from ZrCN–Ag coatings by surface agglomeration mechanism: Structural characterization. *J. Phys. D Appl. Phys.* **2013**, *46*, 325303. [CrossRef]

42.　Powell, C.J. Recommended Auger parameters for 42 elemental solids. *J. Electron. Spectros. Relat. Phenom.* **2012**, *185*, 1–3. [CrossRef]

43.　Turco, A.; Moglianetti, M.; Corvaglia, S.; Rella, S.; Catelani, T.; Marotta, R.; Malitesta, C.; Pompa, P.P. Sputtering-Enabled Intracellular X-ray Photoelectron Spectroscopy: A Versatile Method To Analyze the Biological Fate of Metal Nanoparticles. *ACS Nano* **2018**, *12*, 7731–7740. [CrossRef]

44.　Kaspar, T.C.; Droubay, T.; Chambers, S.A.; Bagus, P.S. Spectroscopic evidence for Ag(III) in highly oxidized silver films by X-ray photoelectron spectroscopy. *J. Phys. Chem. C* **2010**, *114*, 21562–21571. [CrossRef]

45.　Azadmanjiri, J.; Wang, J.; Berndt, C.C.; Kapoor, A.; Zhu, D.M.; Ang, A.S.M.; Srivastava, V.K. Tantalum- and silver-doped titanium dioxide nanosheets film: Influence on interfacial bonding structure and hardness of the surface system. *Ind. Eng. Chem. Res.* **2017**, *56*, 434–439. [CrossRef]

46.　Mori, K.; Saito, T. Effects of stent structure on stent flexibility measurements. *Ann. Biomed. Eng.* **2005**, *33*, 733–742. [CrossRef]

47.　Hu, J.J.; Muratore, C.; Voevodin, A.A. Silver diffusion and high-temperature lubrication mechanisms of YSZ–Ag–Mo based nanocomposite coatings. *Compos. Sci. Technol.* **2007**, *67*, 336–347. [CrossRef]

48. Incerti, L.; Rota, A.; Valeri, S.; Miguel, A.; García, J.A.; Rodríguez, R.J.; Osés, J. Nanostructured self-lubricating CrN-Ag films deposited by PVD arc discharge and magnetron sputtering. *Vacuum* **2011**, *85*, 1108–1113. [CrossRef]

49. Song, D.-H.; Uhm, S.-H.; Lee, S.-B.; Han, J.-G.; Kim, K.-N. Antimicrobial silver-containing titanium oxide nanocomposite coatings by a reactive magnetron sputtering. *Thin Solid Films* **2011**, *519*, 7079–7085. [CrossRef]

50. Fey, P.D.; Olson, M.E. Current concepts in biofilm formation of *Staphylococcus epidermidis*. *Future Microbiol.* **2010**, *5*, 917–933. [CrossRef] [PubMed]

51. O'Gara, J.P.; Humphreys, H. *Staphylococcus epidermidis* biofilms: Importance and implications. *J. Med. Microbiol.* **2001**, *50*, 582–587. [CrossRef] [PubMed]

52. Le, K.Y.; Park, M.D.; Otto, M. Immune evasion mechanisms of *Staphylococcus epidermidis* biofilm infection. *Front. Microbiol.* **2018**, *9*, 359. [CrossRef] [PubMed]

53. Percival, S.L.; Bowler, P.; Woods, E.J. Assessing the effect of an antimicrobial wound dressing on biofilms. *Wound Repair Regen.* **2008**, *16*, 52–57. [CrossRef] [PubMed]

54. Dallas, P.; Sharma, V.K.; Zboril, R. Silver polymeric nanocomposites as advanced antimicrobial agents: Classification, synthetic paths, applications, and perspectives. *Adv. Colloid Interface Sci.* **2011**, *166*, 119–135. [CrossRef] [PubMed]

55. Ferreri, I.; Velasco, S.C.; Galindo, R.E.; Palacio, C.; Henriques, M.; Piedade, A.P.; Carvalho, S. Silver activation on thin films of Ag–ZrCN coatings for antimicrobial activity. *Mater. Sci. Eng. C* **2015**, *55*, 547–555. [CrossRef] [PubMed]

56. Mohamed, D.S.; Abd El-Baky, R.M.; Sandle, T.; Mandour, S.A.; Ahmed, E.F. Antimicrobial activity of silver-treated bacteria against other multi-drug resistant pathogens in their environment. *Antibiotics* **2020**, *9*, 181. [CrossRef]

57. Goderecci, S.S.; Kaiser, E.; Yanakas, M.; Norris, Z.; Scaturro, J.; Oszust, R.; Medina, C.D.; Waechter, F.; Heon, M.; Krchnavek, R.R.; et al. Silver oxide coatings with high silver-ion elution rates and characterization of bactericidal activity. *Molecules* **2017**, *22*, 1487. [CrossRef] [PubMed]

58. Park, H.-J.; Kim, J.Y.; Kim, J.; Lee, J.-H.; Hahn, J.-S.; Gu, M.B.; Yoon, J. Silver-ion-mediated reactive oxygen species generation affecting bactericidal activity. *Water Res.* **2009**, *43*, 1027–1032. [CrossRef] [PubMed]

59. Fang, F.C. Antimicrobial actions of reactive oxygen species. *mBio* **2011**, *2*, e00141-11. [CrossRef]

60. Bull, J.J.; Wilke, C.O. Lethal mutagenesis of bacteria. *Genetics* **2008**, *180*, 1061–1070. [CrossRef]

61. Buckley, A.N.; Woods, R. Identifying chemisorption in the interaction of thiol collectors with sulfide minerals by XPS: Adsorption of xanthate on silver and silver sulfide. *Colloids Surfaces A Physicochem. Eng. Asp.* **1995**, *104*, 295–305. [CrossRef]

62. Hahn, M.M.; Gunn, J.S. *Salmonella* extracellular polymeric substances modulate innate phagocyte activity and enhance tolerance of biofilm-associated bacteria to oxidative stress. *Microorganisms* **2020**, *8*, 253. [CrossRef]

63. Grenho, L.; Salgado, C.L.; Fernandes, M.H.; Monteiro, F.J.; Ferraz, M.P. Antibacterial activity and biocompatibility of three-dimensional nanostructured porous granules of hydroxyapatite and zinc oxide nanoparticles—Anin vitroandin vivostudy. *Nanotechnology* **2015**, *26*, 315101. [CrossRef]

Publisher's Note: MDPI stays neutral with regard to jurisdictional claims in published maps and institutional affiliations.